Supporting Information

Anisotropic Protein Diffusion on Nanosurface

Yang Liu,[a] Xiaohan Song[a], Yanmei Yang,[b]* Yong-Qiang Li[a], Mingwen Zhao,[a]

Yuguang Mu[c]* and Weifeng Li[a]*

[a] *School of Physics and State Key Laboratory of Crystal Materials, Shandong University, Jinan, Shandong, 250100, China*

[b] *College of Chemistry, Chemical Engineering and Materials Science, Collaborative Innovation Center of Functionalized Probes for Chemical Imaging in Universities of Shandong, Key Laboratory of Molecular and Nano Probes, Ministry of Education, Institute of Molecular and Nano Science, Shandong Normal University, Jinan, 250014, China*

[c] *School of Biological Sciences, Nanyang Technological University, 637551, Singapore*

* *Corresponding authors.* yym@sdnu.edu.cn (Y.Y.), *ygmu@ntu.edu.sg* (Y.M.), *lwf@sdu.edu.cn* (W.L.)

1. Force field parameterization

The classical models of MBP and α-PC are developed by fitting to the binding energy curves of two probe molecules (methane and water) from Quantum Mechanics (QM) calculations. The probe molecule was placed 1.0 nm away from the substrate and moved towards the substrate. The structure was optimized by both MD calculation (with steepest descent algorithm in GROMACS) and QM calculation with the Vienna ab initio simulation package (VASP)[1]. In QM calculations, the general gradient approximation (GGA)[2] of Perdew, Burke and Ernzerhof (PBE)[3] is adopted to describe the exchange correlation potential. Energy cutoff of 520 eV is employed for the plane-wave basis. A vacuum larger than 20 Å is used to eliminate the interaction between adjacent images. The Brillouin zone integrations were carried out by the Monkhorst-Pack k-points meshes of 3×3×1.[4] All the structures are fully relaxed with a force tolerance of 0.01 eV/Å. Van der Waals (vdW) functional with D2 Grimme's method[5] is adopted when calculating the non-bonded interactions. All calculations are based on a 3×4×1 supercell of MBP and 2×4×1 supercell of α-PC with periodic boundary conditions. In good agreement with the previous works,[6-8] the lattice parameters of MBP and α-PC are 13.722 Å × 13.224 Å and 17.021 Å × 11.678 Å, respectively.

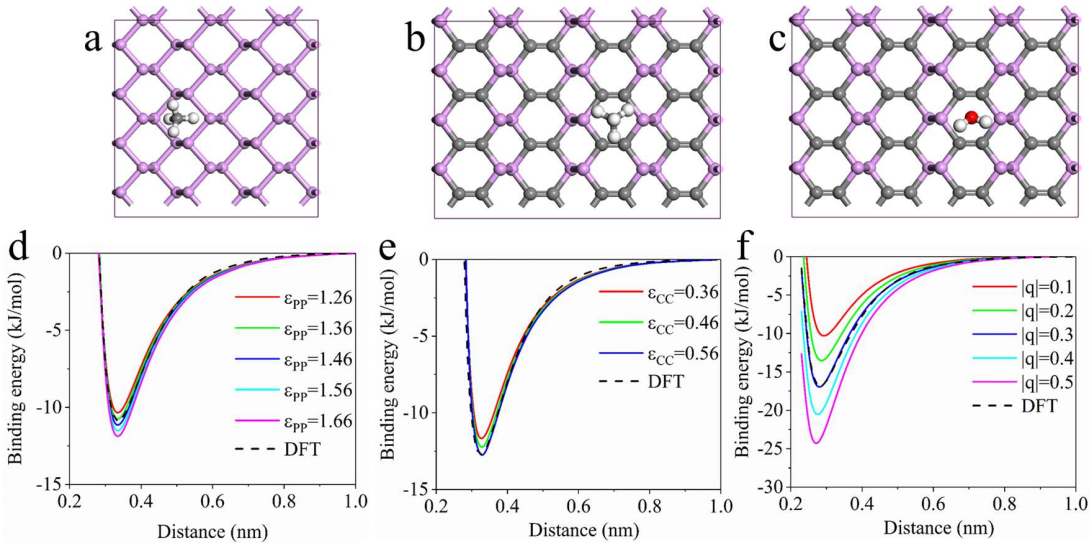

Figure S1. Structure models for MD force field parameterization: (a) a methane molecule adsorbed on MBP; (b) a methane adsorbed on α-PC; (c) a water adsorbed on α-PC. The bottom of each structure depicts the corresponding potential energy curves from QM and MD level calculations.

For the MBP, the P atoms are modeled as Lennard-Jones (L-J) spheres without point charges. The two parameters, σ_P and ε_P, were obtained by fitting methane adsorption process from MD to QM profiles as depicted in Fig. S1a. The initial values of σ_P and ε_P were 0.333 nm and 1.66 kJ/mol, respectively, which were close to the values reported by Ballone and Jones.[9] The methane molecule was described by the AMBER99SB force field. By fitting to the QM curve in Fig. S1d, the optimal values were determined to be σ_P = 0.333 nm and ε_P = 1.36 kJ/mol which well reproduced the QM data.

While for α-PC, the σ_C and ε_C of α-PC were parameterized by fitting the adsorption process of a methane to α-PC (Fig. S1b) while the L-J parameters for P were adopted from MBP directly. The initial values of σ_C and ε_C were adopted from aromatic carbon (CA atom type) in the AMBER99SB force field. After optimization (Fig. S1e), the values were determined to be σ_C = 0.340 nm and ε_C = 0.56 kJ/mol. As the electronegativity difference between P and C atoms causes electron transfer from P to C, the partial charges in α-PC have to be considered explicitly. The partial charges of P (q_P) and C (q_C) were fitted by calculating the binding energy of a water to α-PC (Fig. S1c). Here, the TIP3P water model was used in MD calculations. As depicted in Fig. S1f, the values of q_P = -0.3e and q_C = 0.3e reproduced the QM calculations for the best. The force field parameters are summarized in Table S1 and compatible to AMBER force fields. In constructing the parameter matrix for the non-bonded LJ-parameters, the Lorentz-Berthelot rules should be used.

Table S1. The force field parameters expressed in AMBER format.

	ε (kj/mol)	σ (nm)	q (e)
P (MBP)	1.36	0.333	0
P (α-PC)	1.36	0.333	-0.3
C (α-PC)	0.56	0.340	0.3

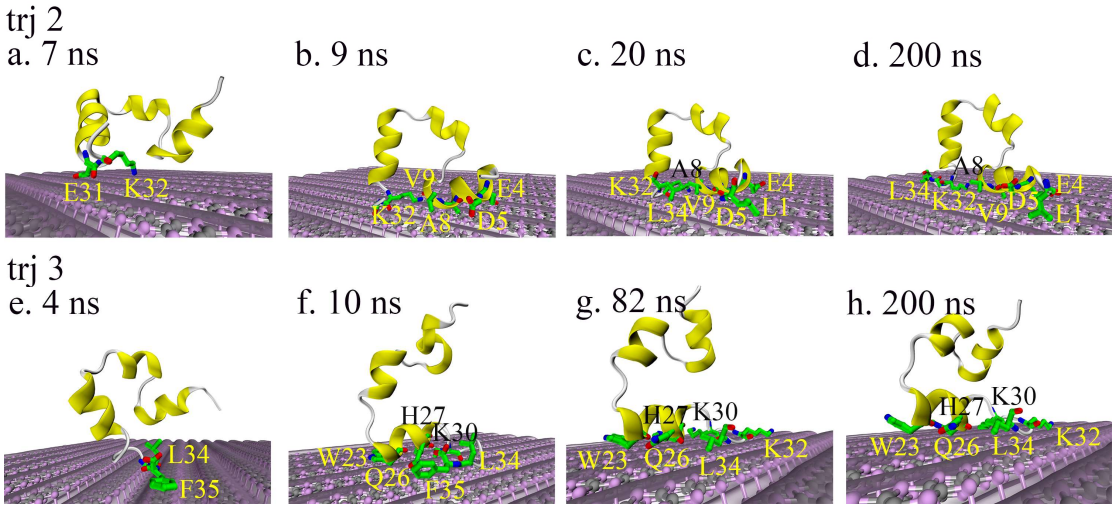

Figure S2. Snapshots of HP35 binding to α-PC in parallel trajectory 2 and 3.

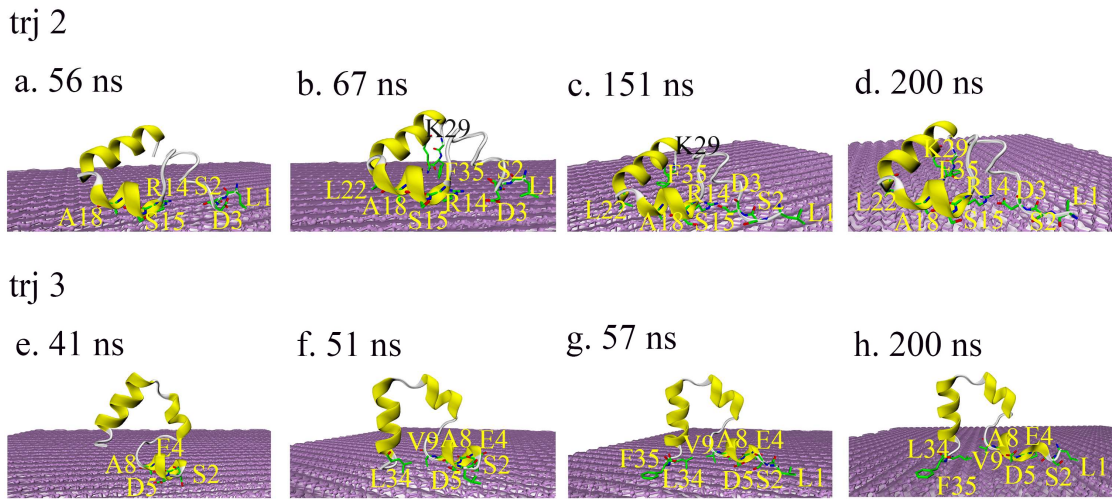

Figure S3. Snapshots of HP35 binding to MBP in parallel trajectory 2 and 3.

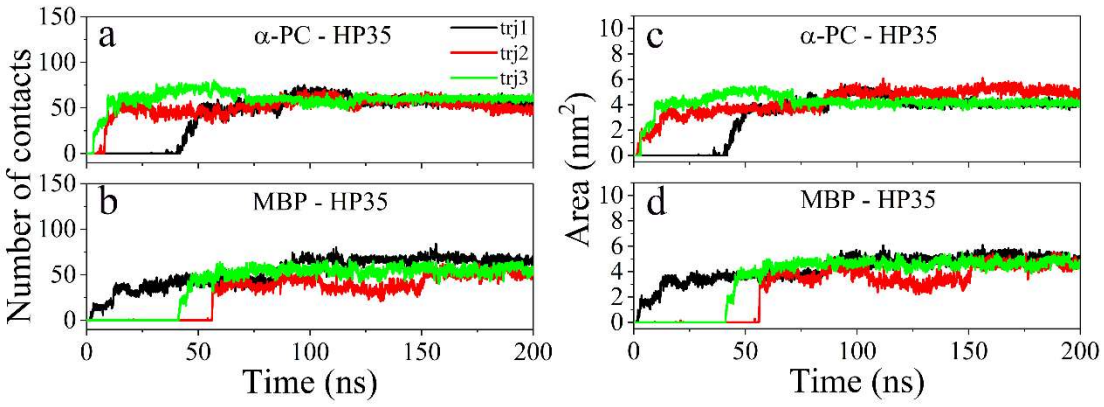

Figure S4. Number of contacts (*N*c) between heavy atoms of HP35 and (a) α-PC or (b) MBP. Contacting surface area of HP35 with (c) α-PC or (d) MBP.

For the calculations of *N*c, a pair of atoms (excluding hydrogen) from HP35 and α-PC/MBP respectively separated within 0.5 nm is treated as a contacting pair. After the initial loading stage, the value of *N*c fluctuates around a value of 50, indicating very stable binding pattern between HP35 and the substrates. The contacting surface area is calculated by $Sc = 0.5 * (S_P + S_N - S_{P+N})$, where S_P, S_N, and S_{P+N} denote the solvent accessible surface area of the protein, nanomaterial and complex, respectively. The profiles of contacting surface area exhibit similar variation tendencies to the corresponding *Nc* profiles.

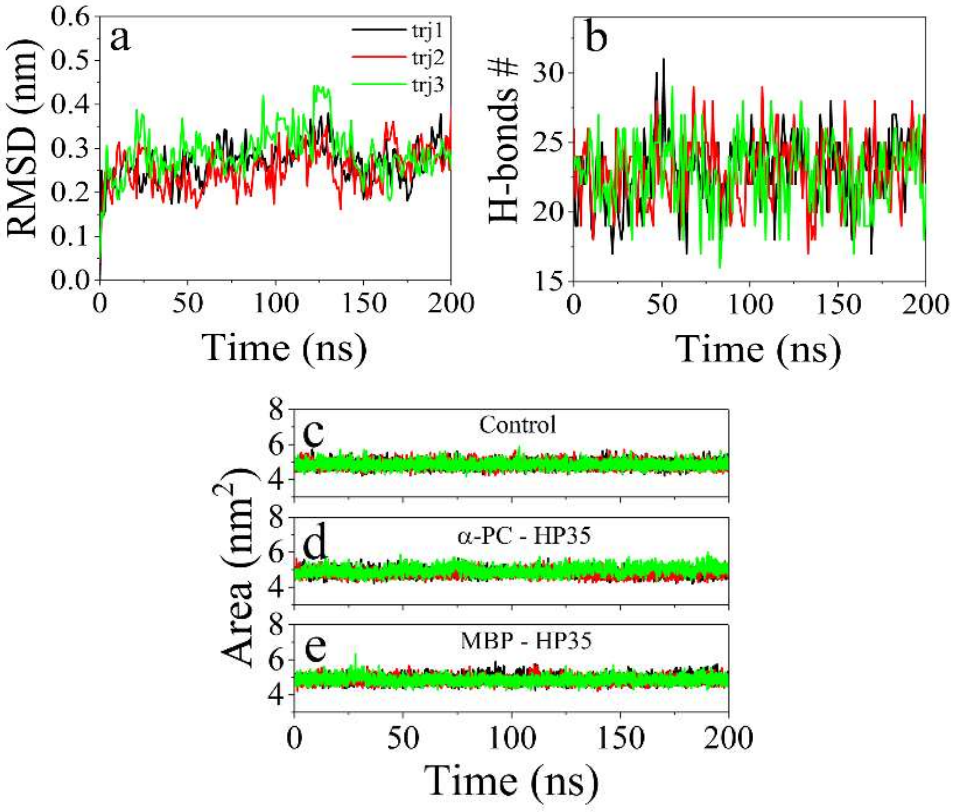

Figure S5. (a) The RMSD of HP35 heavy atoms with respect to the crystal structure and (b) the number of intra-protein H-bonds in the three control simulations of HP35 in water. The solvent accessible surface areas of (c) HP35 in pure water, (d) HP35 binding to α-PC and (e) HP35 binding to MBP.

Here the RMSD converges at 0.28 ± 0.04 nm and number of H-bonds converges at 23.0 ± 2.6 in the control simulations, respectively. The solvent accessible surface area is also well maintained in the simulation. These results reveal a fact that HP35 maintains a stable structure in pure water.

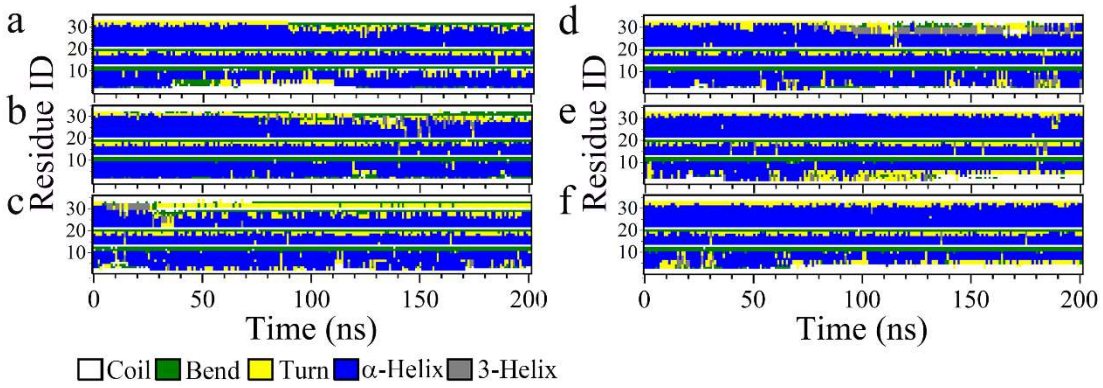

Figure S6. Secondary structure analyses for HP35 upon binding to α-PC (a, b and c for parallel trajectory1, 2 and 3, respectively) and MBP (d, e and f for parallel trajectory1, 2 and 3, respectively).

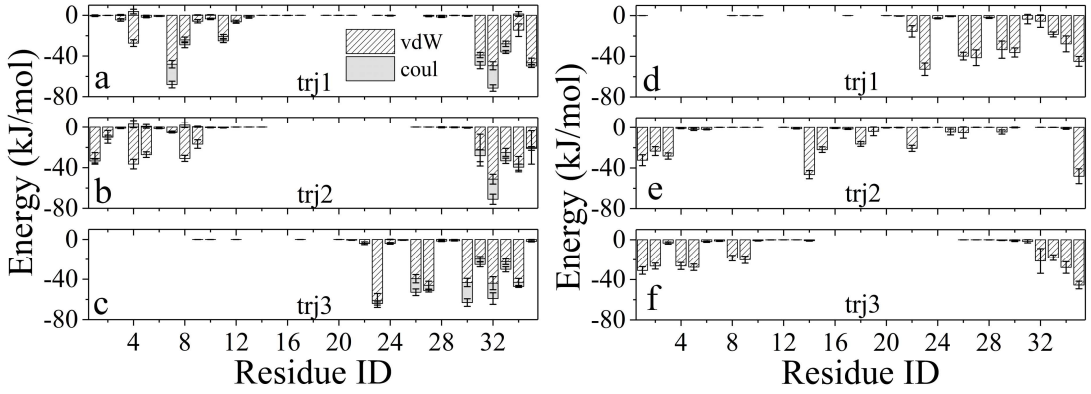

Figure S7. Energy decomposition of the α-PC-HP35 (a, b and c for parallel trajectory1, 2 and 3, respectively) and MBP-HP35 (d, e and f for parallel trajectory1, 2 and 3, respectively).

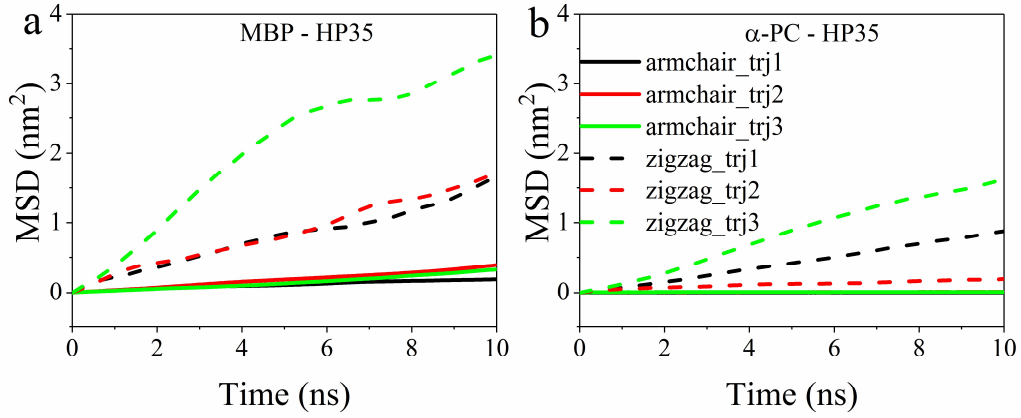

Figure S8. The mean squared displacement (MSD) of HP35 on (a) MBP and (b) α-PC. The MSD values were calculated along the orthogonal armchair and zigzag directions which were represented as solid and dash lines, respectively.

Firstly, it is worth noticing that, the specific MSD values differ in the three parallel simulations for each nanosheet. This is because HP35 adopts different conformations on the nanosheet, resulting in different diffusive character. However, for two nanosheets, the HP35 diffusion along the zigzag direction is always faster than that along the armchair direction in all the simulations. Moreover, from Fig. S8b, it is clear that the diffusion along the armchair direction of α-PC is completely inhibited.

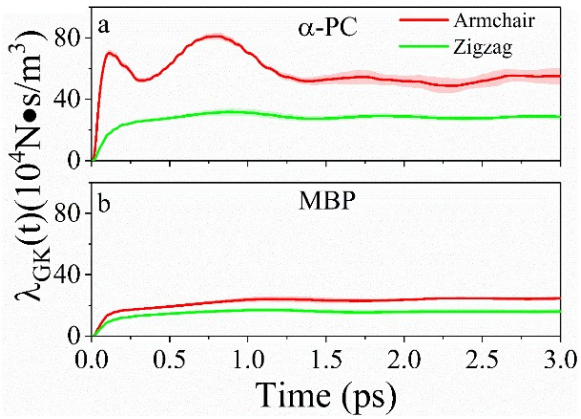

Figure S9. Friction coefficients of water on (a) α-PC and (b) MBP.

To further access the anisotropic diffusion characteristic of HP35 on the two nanosheets, we calculated the friction coefficients of water on α-PC and MBP, respectively. Here, the friction coefficient is estimated based on the Green-Kubo formula $\lambda_{GK}(t) = \frac{1}{2Sk_BT}\int_0^t \langle F_p(t') \cdot F_p(0)\rangle dt'$, where S is the surface area of the substrates, k_B is the Boltzmann constant, T is the temperature (300 K), and F_p is the friction force on water. The factor of 1/2 comes from the contacting from both sides of the substrates. The friction coefficients of α-PC are calculated to be 5.13×10^5 N • s/m^3 (along the armchair direction) and 2.83×10^5 N • s/m^3(along the zigzag direction) respectively. While for MBP, the corresponding values are 2.43×10^5 N • s/m^3 and 1.63×10^5 N • s/m^3. First, for each nanosheet, the friction along the armchair direction is uniformly larger than that along the zigzag direction. Thus adsorbate molecules are expected to diffuse faster along the zigzag direction that that along the armchair direction. These results are well consistent with the MSD analyses in Fig. S8. Second, compared to α-PC, MBP has smaller friction along both the zigzag and armchair directions, indicating that MBP is relatively "smoother" than α-PC.

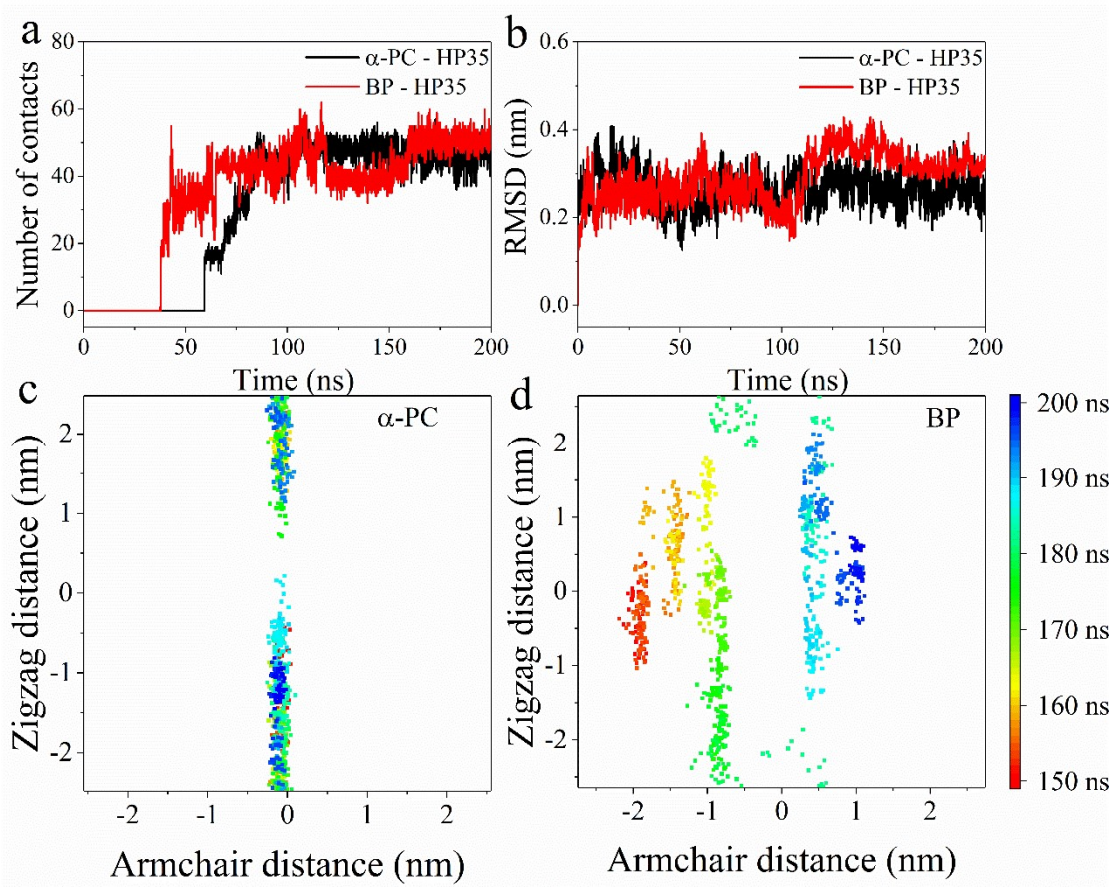

Figure S10. Binding and diffusion of HP35 on five-layer BP and α-PC. Number of contacts between heavy atoms of HP35 and the five-layer substrates as a function of simulation time (a) shows the quick binding process of HP35 to the substrates. Time evolution of HP35 RMSD with respect to its initial structure (b) indicates that the protein's secondary structure is well maintained during the binding. (c) and (d) show the migration path of HP35 on the substrates after the stable binding.

All these figures reveal similar binding behaviors of HP35 to five-layer substrates when compared to the one-layer substrates, indicating that the thickness of substrates have tiny influence to the HP35 binding. Our five-layer models are well-equilibrated by 50 ns MD simulation. The initial distances between neighboring layers are all set to 1 nm. After equilibration, such distances decrease to 0.51 nm for the five-layer BP and 0.52 nm for the five-layer α-PC.

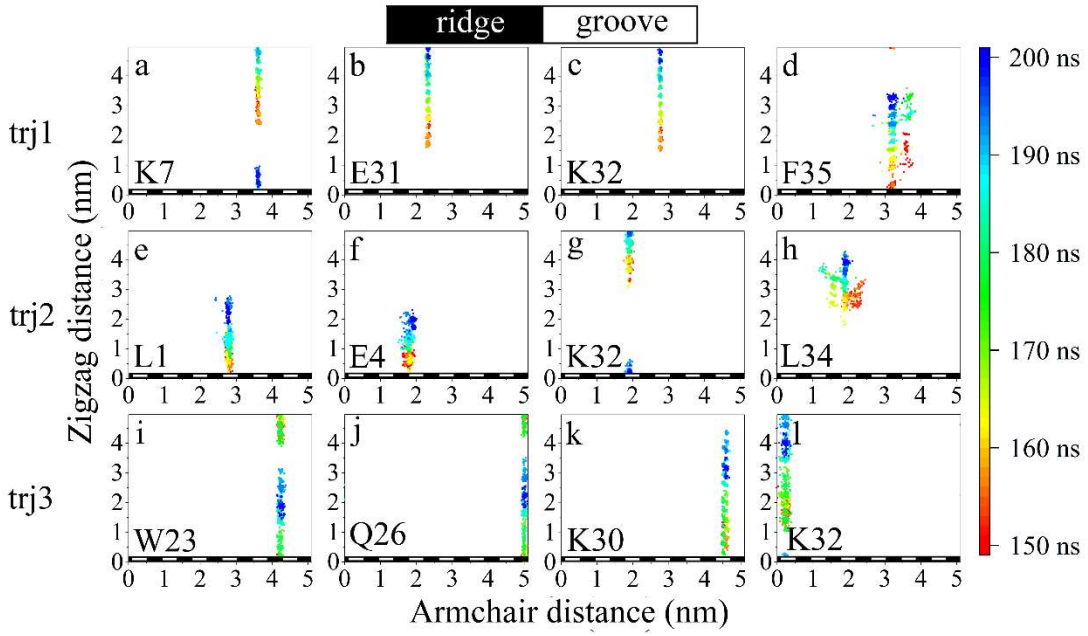

Figure S11. The migration paths of HP35 residues on α-PC after their stable binding (last 50 ns trajectory). Only the first four residues constitute to the total interaction energy in each trajectory are monitored. Each data point represents the center of mass of the residue's sidechain, and is colored chronologically from red to blue. The ridge and groove regions along the armchair direction are labelled on the x-axis with black and white color, respectively.

The behavior of the whole protein is largely decided by its residues contacted with the substrate. To gain a better understanding of such a directional motion of HP35 on α-PC, we divided the whole protein migration down to residues where the first four residues that constitute to the total interaction energy in each trajectory, as summarized in Table S2, were specially monitored as representative residues. The diffusion behaviors of the four residues are shown in Fig. S11. It is interesting to find that the positively charged residues, Lys-7 (Fig. S11a) and Lys-32 (Fig. S11c) in trajectory 1, Lys-32 (Fig. S11g) in trajectory 2, Lys-30 (Fig. S11k) and Lys-32 (Fig. S11l) in trajectory 3, migrate only along the grooves. This is mainly attributed to the electrostatic interactions between the sidechains and the grooves which are negatively charged phosphorus atoms. For the negatively charged residues such as Glu-31 in trajectory 1 (Fig. S11b) and Glu-4 (Fig. S11f) in trajectory 2, they stick to the ridges where the positively charged carbon atoms locate. However, the migration anisotropy of the negatively charged residues is not as obvious as the positively charged residues. For

instance, Glu-4 in trajectory 2 can cross the border line between the ridge and groove frequently although the migration is mainly along the zigzag direction. In addition, the hydrophobic residues, including the aromatic species, also demonstrate the directional migration property along the grooves. For instance, Leu-1 in trajectory 2 (Fig. S11e) and Trp-23 in trajectory 3 (Fig. S11i) demonstrate highly directional migration. However, Phe-35 in trajectory 1 (Fig. S11d) and L34 in trajectory 2 (Fig. S11h) only show certain biased diffusion but not as strong as the two charged residues. The preferential migration of these representative residues is mainly along the grooves, which contributes to the global migration of whole protein. Based on the behaviors of the monitored residues, the positively charged Lys residues play critical roles in determining the directional migration of the whole protein.

Table S2. The percentage contribution of each residue to the interaction energy between HP35 and nanomaterials.

Residues	MBP&HP35 (%)			α-PC&HP35 (%)		
	trj1	trj2	trj3	trj1	trj2	trj3
1L	0	12.12	11.33	0.16	9.51	0
2S	0	8.75	9.7	0.02	2.83	0
3D	0	10.58	1.2	1.05	0.28	0
4E	0	0.35	9.65	6.01	9.48	0
5D	0	0.76	10.12	0.45	7.5	0
6F	0	0.73	0.67	0.26	0.38	0
7K	0	0.01	0.41	17.31	1.51	0
8A	0	0	6.76	7.36	8.19	0
9V	0	0	7.34	1.40	4.65	0
10F	0.01	0	0.28	0.78	0.14	0
11G	0	0	0.01	6.38	0.18	0
12M	0	0	0	1.64	0	0
13T	0	0.47	0	0.41	0	0
14R	0	17.42	0.27	0	0	0
15S	0	8.21	0	0	0	0
16A	0	0.35	0	0.02	0	0
17F	0	0.61	0	0	0	0
18A	0	6.13	0	0	0	0
19N	0	1.48	0	0	0	0
20L	0	0.16	0	0	0	0
21P	0.13	0.1	0	0	0	0.13
22L	4.75	7.75	0	0	0	0.95
23W	16.21	0.07	0	0	0	15.76
24K	0.8	0	0	0.09	0	0.93
25Q	0.25	1.72	0	0	0	0.16
26Q	12.24	1.93	0	0	0	13.03
27H	12.73	0	0	0.19	0	12.62
28L	0.64	0	0	0.41	0.06	0.34
29K	10.29	1.72	0.18	0.02	0.07	0.29
30K	11.15	0.05	0.33	0.2	0.19	15.54
31E	1.05	0	0.56	12.46	8.03	6.21
32K	1.67	0	7.81	18.19	20.24	14.57
33G	5.69	0.02	6.57	9.15	9.47	7.41
34L	8.53	0.46	10.20	3.37	11.25	11.62
35F	13.84	18.03	16.61	12.67	6	0.44

References

1. G. Kresse and J. Furthmüller, *Physical review B*, 1996, **54**, 11169.
2. P. Hohenberg and W. Kohn, *Phys. Rev. B*, 1964, **136**, 864-871.
3. J. P. Perdew, K. Burke and M. Ernzerhof, *Phys. Rev. Lett.*, 1996, **77**, 3865-3868.
4. H. J. Monkhorst and J. D. Pack, *Phys. Rev. B*, 1976, **13**, 5188-5192.
5. S. Grimme, *J. Comput. Chem.*, 2006, **27**, 1787-1799.
6. B. S. Sa, Y. L. Li, J. S. Qi, R. Ahuja and Z. M. Sun, *J. Phys. Chem. C*, 2014, **118**, 26560-26568.
7. W. C. Tan, Y. Cai, R. J. Ng, L. Huang, X. Feng, G. Zhang, Y. W. Zhang, C. A. Nijhuis, X. Liu and K. W. Ang, *Adv. Mater.*, 2017, **29**, 1700503.
8. S. Qi, F. Li, J. Wang, Y. Qu, Y. Yang, W. Li and M. Zhao, *Carbon*, 2019, **141**, 444-450.
9. P. Ballone and R. O. Jones, *J. Chem. Phys.*, 2004, **121**, 8147-8157.